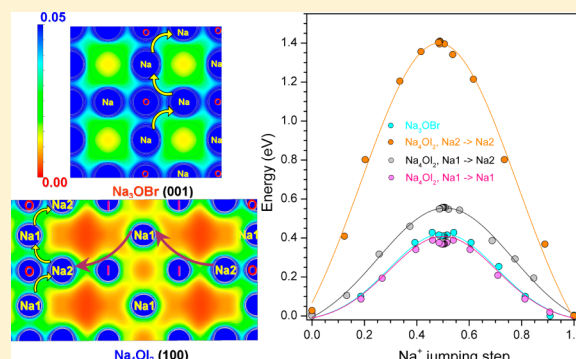


Sodium Ion Transport Mechanisms in Antiperovskite Electrolytes Na_3OBr and Na_4OI_2 : An *in Situ* Neutron Diffraction StudyJinlong Zhu,[†] Yonggang Wang,^{†,‡,§} Shuai Li,[†] John W. Howard,[†] Jörg Neufeind,^{||} Yang Ren,[⊥] Hui Wang,[#] Chengdu Liang,[#] Wenge Yang,^{‡,∇} Ruqiang Zou,^{*,○} Changqing Jin,[◆] and Yusheng Zhao^{*,†}[†]High Pressure Science and Engineering Center, University of Nevada, Las Vegas, Nevada 89154, United States[‡]High Pressure Synergetic Consortium, Geophysical Laboratory, Carnegie Institution of Washington, Argonne, Illinois 60439, United States[§]Institute of Nanostructured Functional Materials, Huanghe Science and Technology College, Zhengzhou, Henan 450006, China^{||}Neutron Scattering Science Directorate, Oak Ridge National Laboratory, 1 Bethel Valley Road, Oak Ridge, Tennessee 37831-6475, United States[⊥]Advanced Photon Source, Argonne National Laboratory, 9700 S. Cass Avenue, Argonne, Illinois 60439, United States[#]Center for Nanophase Materials Sciences, Materials Science and Technology Division, and Chemical Sciences Division, Oak Ridge National Laboratory, Oak Ridge, Tennessee 37831, United States[∇]Center for High Pressure Science and Technology Advanced Research (HPSTAR), Pudong, Shanghai 201203, China[○]Beijing Key Lab of Theory and Technology for Advanced Battery Materials, College of Engineering, Peking University, Beijing 100871, China[◆]National Lab for Condensed Matter Physics, Institute of Physics, Chinese Academy of Sciences, Beijing 100190, China

Supporting Information

ABSTRACT: Na-rich antiperovskites are recently developed solid electrolytes with enhanced sodium ionic conductivity and show promising functionality as a novel solid electrolyte in an all solid-state battery. In this work, the sodium ionic transport pathways of the parent compound Na_3OBr , as well as the modified layered antiperovskite Na_4OI_2 , were studied and compared through temperature-dependent neutron diffraction combined with the maximum entropy method. In the cubic Na_3OBr antiperovskite, the nuclear density distribution maps at 500 K indicate that sodium ions hop within and among oxygen octahedra, and Br^- ions are not involved. In the tetragonal Na_4OI_2 antiperovskite, Na ions, which connect octahedra in the *ab* plane, have the lowest activation energy barrier. The transport of sodium ions along the *c* axis is assisted by I^- ions.



INTRODUCTION

Medium- and large-scale stationary batteries are needed to match production and energy consumption from renewable sources like solar, wind, hydraulic electrogeneration, or even off-peak electrical energy from traditional power stations¹ in a safe, cost-affordable, and sustainable way. In portable electronic devices, lithium-ion batteries are currently the predominantly used secondary cell. The low abundance of lithium on Earth, combined with a continuously increasing demand, provides a formidable future challenge.² While lithium-based rechargeable batteries have the advantage of high energy density and durability,^{3–5} the sodium ion battery^{6,7} has a potential advantage when considering raw material abundance and cost. Today three types of sodium ion batteries are mainly used: the Na–S battery, which requires molten sodium and sulfur at 300–350 °C,^{7,8} the organic liquid electrolyte-based battery,⁹ and aqueous sodium ion batteries.^{10–12} In nonaqueous

sodium ion batteries, replacing the liquid or polymeric organic electrolyte^{13–15} with a cheap, safe, and stable solid electrolyte^{16–20} will reduce the risk of leakage and ignition, as well as reducing cost. Currently, the existing sodium solid electrolytes can be broadly categorized into chalcogenides^{17,18} and the Na super ionic conductor (NASICON);^{19,20} the latter suffers from a high grain-boundary resistance, which requires elevated sintering temperatures to overcome. Exploration of a new class of sodium solid electrolyte candidates could not only enhance the flexibility of full solid-state battery design, but also contribute to the requirements of large-scale energy storage and transportation in a safe and environmental friendly way.

The recent development of the antiperovskite electrolyte family^{21,22} derived from perovskites NaMgF_3 and $(\text{K},\text{Na})\text{MgF}_3$

Received: February 26, 2016

Published: June 2, 2016

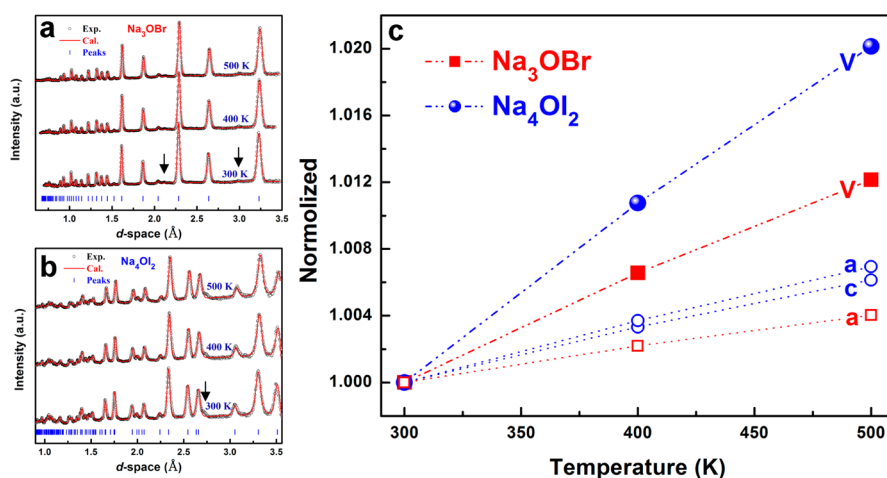


Figure 1. Neutron diffraction patterns of (a) Na_3OBr and (b) Na_4OI_2 at 300, 400, and 500 K ($2\theta = 66^\circ$). The experimental data are in black circles, the Rietveld fitting is the red line, and the blue ticks represent the peak positions; the arrows at 2.2 and 3.0 Å in part a indicate the peak positions of impurity NaBr phase, and the peak at ~ 2.7 Å in part b could come from some Na–O–I polymorph. (c) Normalized volumes and lattice parameters of Na_3OBr and Na_4OI_2 as a function of temperature in the range 300–500 K; Na_4OI_2 has an average thermal expansion coefficient of $10.1(4) \times 10^{-5} \text{ K}^{-1}$, larger than that for Na_3OBr $6.1(3) \times 10^{-5} \text{ K}^{-1}$. In the Na_4OI_2 structure, the thermal expansion along the a axis is larger than in the c axis direction.

Table 1. Refined Crystal Parameters for Na_3OBr and Na_4OI_2 at 300, 400, and 500 K^a

formula	lattice params (Å)		coordinates of equivalent positions				thermal params		
			x	y	z	occupancy	U_{11}	U_{22}	U_{33}
Na_3OBr	$a = 4.5674(1)$ 300 K	Na	0.5	0	0.5	0.989(2)	0.015	0.033	0.033
	$a = 4.5774(1)$ 400 K					0.990(4)	0.016	0.039	0.039
	$a = 4.5858(3)$ 500 K					0.992(6)	0.018	0.044	0.044
		O	0.5	0.5	0.5	0.995(1)	$U_{\text{iso}} = 0.018/0.024/0.027$		
						0.996(4)			
						0.995(7)			
		Br	0	0	0	1.0	$U_{\text{iso}} = 0.010/0.011/0.013$		
Na_4OI_2	$a = 4.6902(3)$ 300 K	Na1	0	0.5	0	0.965(3)	0.031	0.027	0.049
	$c = 16.0086(10)$					0.961(4)	0.040	0.026	0.061
	$a = 4.7053(3)$ 400 K					0.964(3)	0.044	0.032	0.076
	$c = 16.0536(12)$	Na2	0	0	0.1425(1)	1.0	0.040	0.040	0.033
	$a = 4.6729(1)$ 500 K					0.1425(3)	0.049	0.049	0.039
	$c = 15.9556(5)$					0.1422(3)	0.062	0.062	0.044
		O	0	0	0	0.983(2)	$U_{\text{iso}} = 0.018/0.022/0.027$		
						0.980(5)			
						0.982(3)			
		I	0	0	0.3468(2)	1.0	$U_{\text{iso}} = 0.019/0.025/0.032$		
					0.3466(3)				
					0.3466(1)				

^aThe defect vacancies are both from Na_2O with $\sim 1\%$ Na^+ vacancies in Na_3OBr and $\sim 3.5\%$ Na^+ vacancies in Na_4OI_2 . The refined Rwp (Rp) for Na_3OBr at 300, 400, and 500 K are 3.30% (2.54%), 3.02% (2.48%), and 4.02% (2.69%), respectively; those for Na_4OI_2 at 300, 400, and 500 K are 4.01% (3.22%), 3.78% (2.93%), and 3.28% (2.48%), respectively. Firstly, all atomic occupancies were refined, and the results indicated that the occupancies of the halide sites and Na2 site stayed at 1, the others had occupancies less than 1; the occupancies of the halide sites and Na2 site were fixed during the following refinement.

could be promising due to their structural tolerance and superionic conductivity. For example, through aliovalent substitution, the ionic conductivity of the compound $\text{Na}_{2.9}\text{Sr}_{0.05}\text{OBr}_{0.6}\text{I}_{0.4}$ reached 0.19 S m^{-1} at 200°C .²² However, fundamental scientific information, such as sodium ion transport and kinetic properties, must be obtained to successfully guide the synthesis of new Na-rich antiperovskites that perform at or above the desired level. Thus, an experimental investigation on the ionic transport mechanism within various antiperovskite-type electrolyte materials and an in-depth understanding of the structure–property relationship

should be significant for future development of such antiperovskite materials. In this work, Na_3OBr ²³ and Na_4OI_2 ²⁴ have been studied as two representatives of Na-rich antiperovskites for sodium ion transport investigations. These particular structures, albeit not with optimal ionic conductivities, have been selected to extract the fundamental transport mechanism without the confounding effects of doping or substitution, and to compare the transport in two distinct classes of antiperovskite crystals. Impedance spectroscopy and powder neutron diffraction measurements were performed as a function of temperature to study the sodium ionic con-

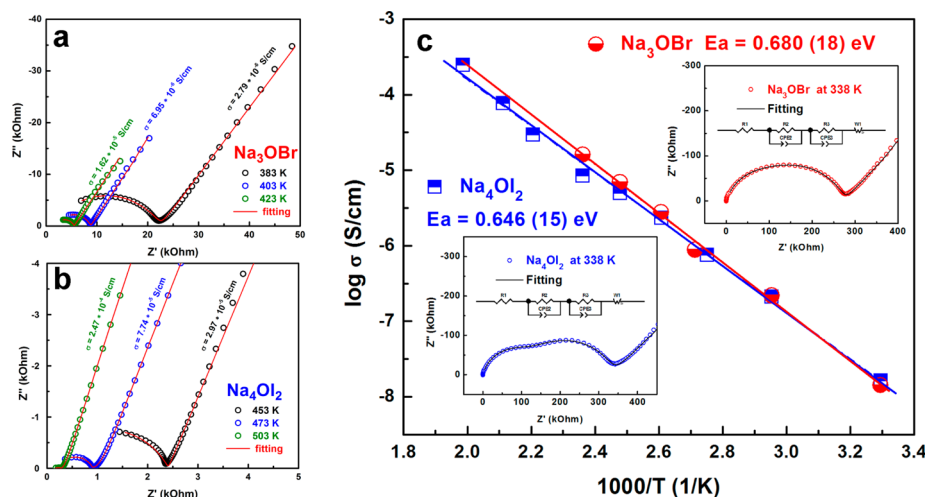


Figure 2. Impedance spectroscopy Nyquist plots of (a) Na_3OBr and (b) Na_4OI_2 measured at different temperatures. The symmetric cells were made with Au as electrodes, and samples were melted in between. (c) Sodium ionic conductivities of Na_3OBr and Na_4OI_2 as a function of temperature from room temperature to 500 K. The activation energies for Na_3OBr and Na_4OI_2 are 0.680(18) and 0.646(15) eV, respectively.

ductivities and the potential Na^+ transport pathways. The results provide new insight into the future design of these antiperovskites. Chemical manipulations such as elemental doping, size-mismatch replacement, internal/external stresses, and structural manipulations may lead to enhanced sodium ionic conductivity to meet practical application demands.

RESULTS AND DISCUSSIONS

Figure 1 a,b shows the neutron diffraction patterns ($2\theta = 66^\circ$) of Na_3OBr and Na_4OI_2 at 300, 400, and 500 K, respectively. At room temperature (RT), Na_3OBr crystallizes into the cubic antiperovskite structure with space group $Pm\bar{3}m$ and $a = 4.5674(1)$ Å. The lattice is characterized by corner-sharing ONa_6 octahedra with Br^- ions located on the A-site.²³ The layered intergrowth K_2NiF_4 -type Na_4OI_2 is a tetragonal antiperovskite with space group $I4/mmm$ and lattice parameters $a = 4.6729(1)$ Å and $c = 15.9556(5)$ Å. The lattice is characterized by “ Na_3OI ” antiperovskite slabs and “ NaI ” rock-salt layers.²⁴ All the refined parameters are listed in Table 1. The refined volume of Na_3OBr as a function of temperature gives an averaged thermal expansion coefficient of $6.1(3) \times 10^{-5} \text{ K}^{-1}$, while Na_4OI_2 has a slightly larger value of $10.1(4) \times 10^{-5} \text{ K}^{-1}$ with an anisotropic thermal expansion that is 11.5% greater along the a axis than along the c axis, as shown in Figure 1c. The larger expansion along the a axis could be the result of the dense packing in that direction. The two compounds are both nonstoichiometric. The defect vacancies are both from Na_2O with $\sim 1\%$ Na^+ vacancies in Na_3OBr and $\sim 3.5\%$ Na^+ vacancies in Na_4OI_2 , and the divalent oxygen anion balances the charge. These findings indicate that, at least in the sodium antiperovskite, the Na_2O Schottky defects are dominant compared to the lithium halogen Schottky defects in the lithium antiperovskite proposed in a recent theoretical investigation.²⁵ Also, the calculation results indicate that the Na_2O defects are nearest neighbors which minimizes the hopping energy.²⁶ There were no phase transitions for these two phases with temperature up to 500 K. In this temperature range, the ionic conductivities of Na_3OBr and Na_4OI_2 were measured, and the representative impedance curves were plotted in Figure 2 a,b. The relatively low ionic conductivity at room temperature can be effectively enhanced by aliovalent

ion doping at sodium sites. This enhancement is due to large distortion of the lattice by ion replacement as well as an increase in vacancy concentration.²² The sodium transport activation energy of 0.646(15) eV in Na_4OI_2 is lower relative to that of 0.680(18) eV in Na_3OBr (Figure 2c).²⁶ The value is consistent with previous results,²² and higher than that of the Li-counterpart in both bulk²¹ and thin-film forms.²⁷ In the temperature range studied, the ionic conductivity of Na_4OI_2 is comparable to that of Na_3OBr , which is mainly from the similarities in NaI–NaI jumping energies, despite the different bonding strengths and interstitial geometries of the two antiperovskite structures.

In both sodium antiperovskite compounds, the Na^+ ions are bonded to the O^{2-} ions forming ONa_6 octahedra. The octahedra in cubic Na_3OBr are connected to each other at the vertices, forming a three-dimensional (3D) octahedral array. The Br^- ions lie in the center of the eight nearest sodium octahedra. The octahedra in tetragonal Na_4OI_2 are also connected at the vertices in the ab plane, and the octahedra in the (001) and (002) planes relatively shift (1/2, 1/2, 0) each other with NaI layers separating the octahedral layers. The Na atoms in Na_3OBr are crystallographically equivalent.²⁸ Cation transport in isostructural Na_3OBr occurs among nearest-neighbored Na^+ sites (Na–Na atomic distance 3.2297(6) Å at RT) and vacancies along the edges^{28–31} within the ONa_6 octahedra, and through the oxygen ions as shown in Figure 3a and Figure 4. The missing overlap in the nuclear densities of sodium cations and bromine ions (Figure 3b) indicates that bromine ions are not involved in the Na^+ ion migration process. This can be explained by the fact that the Na–O bond length is 2.2837(1) Å, and the Na–Br bond is 3.2296(1) Å at RT, with each O^{2-} ion carrying two electrons.

In contrast, in Na_4OI_2 there are two inequivalent Na positions in the structure, the one at (0, 0.5, 0) is denoted as Na1, and the other at (0, 0, z) is denoted as Na2; three possible sodium migration pathways are proposed: Na1–Na1 (3.3042(4) Å at RT), Na1–Na2 (3.2603(1) Å at RT) with the highest probability, and Na2–Na2 (4.7627(3) Å at RT) with the smallest migration probability. Therefore, differences in the sodium transport behaviors of Na_3OBr and Na_4OI_2 are expected. Na^+ ions at Na1 position have a similar transport mechanism (in the ab plane) as in the Na_3OBr system, which is

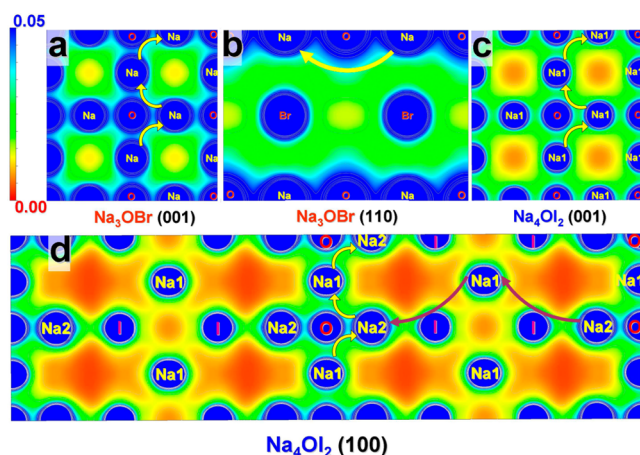


Figure 3. Nuclear density distributions of Na_3OBr and Na_4OI_2 at 500 K deduced from MEM analysis. The isosurface level is between 0 and $0.05 \text{ fm} \text{ \AA}^{-3}$ in (001), (110) planes of Na_3OBr and (001), (100) planes of Na_4OI_2 . The arrows indicate the preferable pathways in both structures, and the two colored arrows in Na_4OI_2 suggest the two transport mechanisms in the ab plane and along the c direction of the layered structure.

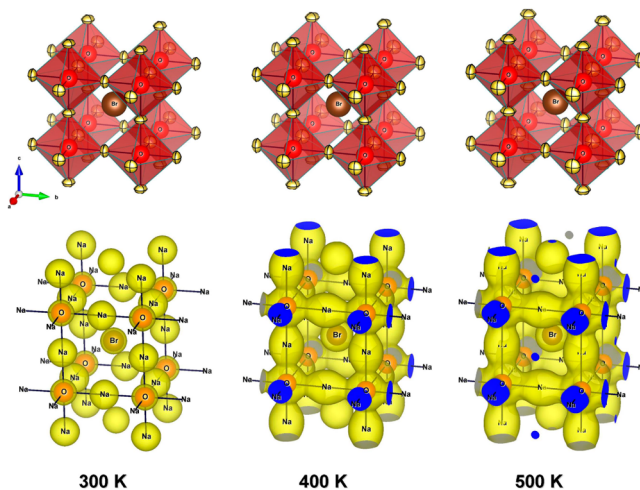


Figure 4. Upper panel shows the schematic crystal structure of Na_3OBr at 300, 400, and 500 K (from left to right) with anisotropic thermal vibration of sodium atoms at 80% probability; lower panel gives the nuclei density distributions from MEM analysis with an isosurface level of $0.03 \text{ fm} \text{ \AA}^{-3}$.

expected as the vertex-to-vertex connection geometry is similar. The sodium ions at the Na1 position show an elliptic-type nuclear density in the ab plane, and have a smaller overlap with oxygen at 500 K as indicated in Figure 3c and Figure 5. The smaller overlap of the Na1 ions and O^{2-} ions is mainly due to the larger Na1–O bond length of $2.3364(1) \text{ \AA}$ as compared to that of the Na–O bond length $2.2837(1) \text{ \AA}$ in the Na_3OBr crystal. Furthermore, there is no obvious interaction between Na2 ions and I^- ions in the ab plane, similar to the Na^+ and Br^- ions in Na_3OBr (Figure 3b). The anisotropic effect in tetragonal Na_4OI_2 is mainly expressed in the c direction. As the activation energy of the nearest Na2–Na2 diffusion pathways (along c axis) is $>1 \text{ eV}$, and likely too great to overcome, the possibility of sodium ion transport along the c axis could be via the I^- ion. As shown in the (100) projected planes in Figure 3d and Figure 5, Na^+ ions at the Na2 position

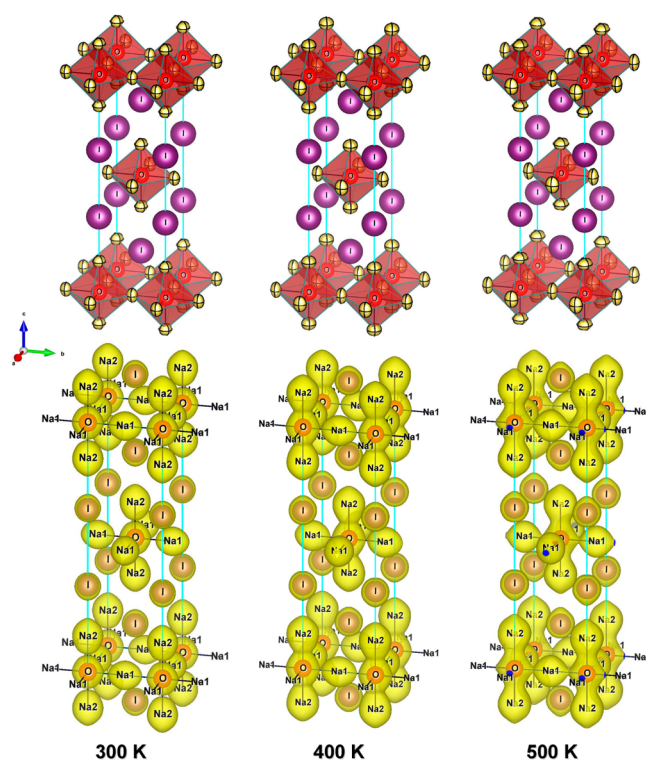


Figure 5. Upper panel shows the schematic crystal structure of Na_4OI_2 at 300, 400, and 500 K (from left to right) with anisotropic thermal vibration of sodium atoms at 80% probability; lower panel gives the nuclei density distributions from MEM analysis with an isosurface level of $0.03 \text{ fm} \text{ \AA}^{-3}$.

exhibit an elliptic nuclear density along the c direction, which overlaps with the I^- ions nuclear densities polarized toward the Na2 ion. This indicates that sodium ions have some likelihood to migrate among different octahedra along the c axis, even though it is a minor migration probability compared with other directions. Interestingly, the polarized nuclear density distribution of the I^- ion, and its overlap with Na2 ion as shown in Figure 3d, strongly suggests that the I^- ion, not only the O^{2-} ion, acts as a pathway of a negative charge center facilitating sodium cation transport in the c direction. It is expected that the ionic conductivity of Na_4OI_2 will be enhanced by doping with smaller radius anions, such as Br^- , Cl^- , or F^- , at the I^- sites to shorten the jump distance of Na^+ ions between isolated octahedra. This ultimately corresponds to a reduction in the energy barrier bottleneck along the c axis.

The increase of ionic radius from Br^- to I^- results in different crystal structure stabilizations. As stated above, the main difference of the cubic and layered sodium antiperovskites (Figure 6a,b) is an intercalation of a NaI layer between Na_3OI layers, producing the isolated ONa_6 octahedra along the c direction. To understand the sodium migration mechanism more clearly in these two antiperovskite systems, especially in the Na_4OI_2 structure, a theoretical model was constructed to simulate the process (Figure 6c). Na_3OBr has a Na–Na migration energy of about 0.34 eV and is isotropic. In contrast, the Na_4OI_2 exhibits three different sodium migration energies with the greatest value of 1.1 eV between nearest Na2 atoms, which is nearly three times larger than that of the other two jumping pathways. Thus, the sodium migration can be considered to be mainly inside the “ Na_3OI ” layer and has an anisotropic transport feature. From the viewpoint of crystal

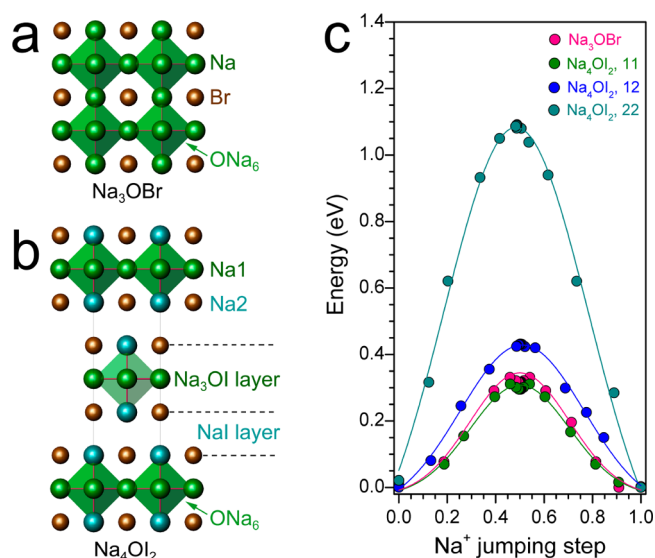


Figure 6. Crystal structures of (a) Na_3OBr and (b) Na_4OI_2 with three-dimensional and layered intergrowth antiperovskites, respectively. (c) Sodium ion jumping energies through different transport routes (11, between Na1 and Na1; 12, between Na1 and Na2; 22, between Na2 and Na2).

structural geometry, the large Na2–Na2 migration energy mainly comes from the large physical distance between sites. It should be noted that Na1 atoms in these two structures both have four nearest halide anions, with four Br^- ions in Na_3OBr and four I^- ions in Na_4OI_2 , leading to the similar migration energies of Na1–Na1 in each structure. Although nearly equivalent, the Na1–Na1 jump energy in Na_4OI_2 (0.3 eV) is slightly smaller than that of Na_3OBr (0.34 eV), which is mainly attributed to the greater ionic radius of the I^- ion and the slightly weaker electrostatic interaction with the anions than that in the Na_3OBr phase. Na2 has four nearest I^- ions in the ab plane of Na_4OI_2 ($\text{Na2}-I_{ab} = 3.3086(4)$ Å), and one nearest neighbor I^- ion along the c axis of Na_4OI_2 ($\text{Na2}-I_c = 3.2599(1)$ Å). The relatively large migration energy for Na2–Na1 (0.45 eV) in Na_4OI_2 is primarily due to the negative electrostatic attraction of Na2, hindering the migration of sodium ions at Na2 sites.

In conclusion, the main sodium transport pathway in both cubic Na_3OBr and layered Na_4OI_2 is between the nearest Na^+ ions in the NaO_6 octahedra building block of the antiperovskite. The polarized nuclear densities of I^- ions bridges the Na^+ ions jumping pathway between two isolated octahedra along the c axis of the layered antiperovskite. The family of sodium-rich solid electrolytes based on the antiperovskite shows promising potential in electrochemical systems through further structural manipulations, chemical manipulations, and stress engineering to optimize the Na^+ ions transport pathways and maximize the ionic conductivity.

EXPERIMENTAL METHODS

Na-rich antiperovskites of Na_3OBr and Na_4OI_2 have been synthesized via a solid-state reaction.²² The 0.05 mol portions of Na_2O and NaBr (for Na_4OI_2 : 0.05 mol Na_2O and 0.1 mol NaI) were weighed and ground for 20 min into well-mixed powder in an argon protected glovebox; the fine powder then was placed in a capped alumina crucible. The mixture was then heated in a compact furnace inside the same glovebox with a heating rate of 1.5 °C/min to 150 °C and then to 400 °C at a heating rate of 10 °C/min. Further reaction details can

be found in ref 22. The entire reaction takes place under argon gas protection. The oxygen and moisture levels were both less than 10 ppm. The reaction is driven at 400 °C for 4 h, following the reaction pathway shown in Equations 1 and 2, and the products were subsequently allowed to cool to room temperature naturally.



Fresh Na_2O is premade by reacting equal moles of Na metal with NaOH at 300 °C. Since the products are moisture sensitive, a 3% excess Na was employed to guarantee the anhydrous state of the products.

As both the electrolytes are moisture- and air-sensitive, electrochemical impedance spectra (EIS) were performed inside the same glovebox as the synthesis. The samples were melted between two pieces of Au foil electrodes forming symmetric cells. The cells were kept for 30 min after reaching the targeted temperature in a compact furnace at each set point before impedance measurement. A Solartron 1260A impedance/gain-phase analyzer was used for the EIS measurements with an applied ac voltage of 10 mV in a frequency range from 1 MHz to 1 Hz.

Time-of-flight (TOF) neutron powder diffraction was performed at NOMAD (Nanoscale-Ordered Materials Diffractometer), SNS (Spallation Neutron Source), Oak Ridge National Laboratory.³² The samples were loaded in quartz capillaries with a diameter of 1 mm. About 2 cm length powder samples were loaded in the quartz capillary inside an argon protected glovebox, and then the capillary was sealed. The Cobra cryostream heating system was used to change temperature from 300 to 500 K. The advantage of using neutron diffraction at NOMAD is that neutron diffraction is not atomic-number-dependent and therefore can get a more accurate determination of the oxygen position than with X-ray diffraction. Additionally, multibank diffraction at NOMAD can cover larger d spacings with higher resolution. To map the sodium ion transport pathways, the nuclear density distributions of Na_3OBr and Na_4OI_2 solid electrolytes over a range of temperatures were analyzed by a MEM/Rietveld refinement technique using data from five detector banks at $2\theta = 154^\circ$, 122° , 66° , 30° , and 15° to gain the maximum d spacing range coverage as well as the high resolution at lower d spacings. The corresponding maximum d -spacing is in the range 0.5–9 Å (Supporting Information Figure S1). The observed structure factors, F_o , and standard uncertainties, $|F_o|$, were estimated with Alchemy³³ from relevant data in files output by GSAS+EXPGUI^{34,35} and analyzed by the MEM with Dynomia.³⁶ The unit cells of Na_3OBr and Na_4OI_2 were divided into $100 \times 100 \times 100$ voxels and $100 \times 100 \times 300$ voxels, respectively. The detailed method for MEM analysis can be found in ref 33.

Sodium migration simulations were performed using CASTEP software³⁷ (LST/QST) at the GGA level of theory. The crystal structures and lattice parameters of Na_3OBr and Na_4OI_2 from neutron diffraction refinements were employed as the initial structure model to study the sodium migration within the two materials. For Na_3OBr , a cubic $2 \times 2 \times 2$ supercell of the perovskite unit cell containing 40 atoms was used to calculate the sodium migration enthalpy. While for Na_4OI_2 , a $2 \times 2 \times 1$ supercell containing 56 atoms was used. Sodium vacancies were generated by artificially removing one of the sodium atoms within the supercell. The shortest pathway for sodium ion was generated automatically from one Na site to the nearest vertex of ONa_6 octahedron (vacancy). During the whole calculation process, the lattice vectors of the supercell were constrained to retain cubic symmetry, but internal ionic relaxations were allowed.

ASSOCIATED CONTENT

Supporting Information

The Supporting Information is available free of charge on the ACS Publications website at DOI: 10.1021/acs.inorgchem.6b00444.

Listings of multibank diffractions (PDF)

AUTHOR INFORMATION

Corresponding Authors

*E-mail: rzou@pku.edu.cn.

*E-mail: yusheng.zhao@unlv.edu.

Author Contributions

J.Z. and Y.W. contributed equally to this work. J.Z., R.Z., and Y.Z. conceived the work. Y.W. synthesized the samples. J.Z. conducted the neutron diffraction experiment with the help of J.N. S.L. and H.W. conducted the impedance measurement with the help of C.L. J.Z. did the MEM analysis and analyzed the data; J.Z. and Y.W. drafted the manuscript. J.Z., J.W.H., J.N., Y.R., C.J., R.Z., W.Y., and Y.Z. helped edit the manuscript and also provided input for the discussion.

Notes

The authors declare no competing financial interest.

ACKNOWLEDGMENTS

We thank the High Pressure Science and Engineering Center (HiPSEC), University of Nevada, Las Vegas, for support. This research was sponsored in part by the National Nuclear Security Administration under the Stewardship Science Academic Alliances program through DOE Cooperative Agreement #DE-NA0001982. A portion of this research at ORNL's Spallation Neutron Source was sponsored by the Scientific User Facilities Division, Office of Basic Energy Sciences, US Department of Energy. We acknowledge the support from NSF & MOST of China through research projects at Institute of Physics, Chinese Academy of Sciences. W.Y. acknowledges the financial support from DOE-BES X-ray Scattering Core Program under Grant DE-FG02-99ER45775.

REFERENCES

- (1) Dunn, B.; Kamath, H.; Tarascon, J. M. *Science* **2011**, *334*, 928–935.
- (2) http://en.wikipedia.org/wiki/File:Elemental_abundances.svg.
- (3) Armand, M.; Tarascon, J.-M. *Nature* **2008**, *451*, 652–657.
- (4) Goodenough, J. B.; Park, K.-S. *J. Am. Chem. Soc.* **2013**, *135*, 1167–1176.
- (5) Marom, R.; Amalraj, S. F.; Leifer, N.; Jacob, D.; Aurbach, D. *J. Mater. Chem.* **2011**, *21*, 9938–9954.
- (6) Pan, H.; Hu, Y.-S.; Chen, L. *Energy Environ. Sci.* **2013**, *6*, 2338–2360.
- (7) Ellis, B. L.; Nazar, L. F. *Curr. Opin. Solid State Mater. Sci.* **2012**, *16*, 168–177.
- (8) Hueso, K. B.; Armand, M.; Rojo, T. *Energy Environ. Sci.* **2013**, *6*, 734–749.
- (9) Ponrouch, A.; Monti, D.; Boschini, A.; Steen, B.; Johansson, P.; Palacin, M. R. *J. Mater. Chem. A* **2015**, *3*, 22–42.
- (10) Whitacre, J. F.; Tevar, A.; Sharma, S. *Electrochem. Commun.* **2010**, *12*, 463–466.
- (11) Li, Z.; Young, D.; Xiang, K.; Carter, W. C.; Chiang, Y.-M. *Adv. Energy Mater.* **2013**, *3*, 290–294.
- (12) Kim, H.; Hong, J.; Park, K.-Y.; Kim, H.; Kim, S.-W.; Kang, K. *Chem. Rev.* **2014**, *114* (23), 11788–11827.
- (13) Knauth, P. *Solid State Ionics* **2009**, *180*, 911–916.
- (14) Tarascon, J.-M.; Armand, M. *Nature* **2001**, *414*, 359–367.
- (15) Ponrouch, A.; Marchante, E.; Courty, M.; Tarascon, J. M.; Palacin, M. R. *Energy Environ. Sci.* **2012**, *5*, 8572–8583.
- (16) Kummer, J. T.; Weber, N. *SAE Tech. Pap. Ser.* **1968**, *76*, 1003–1005.
- (17) Hong, H. Y. P. *Mater. Res. Bull.* **1976**, *11*, 173–182.
- (18) Goodenough, J. B.; Hong, H. Y. P.; Kafalas, J. A. *Mater. Res. Bull.* **1976**, *11*, 203–220.
- (19) Bohnke, O.; Ronchetti, S.; Mazza, D. *Solid State Ionics* **1999**, *122*, 127–136.
- (20) Hayashi, A.; Noi, K.; Sakuda, A.; Tatsumisago, M. *Nat. Commun.* **2012**, *3*, 856.
- (21) Zhao, Y.; Daemen, L. L. *J. Am. Chem. Soc.* **2012**, *134*, 15042–15047.
- (22) Wang, Y.; Wang, Q.; Liu, Z.; Zhou, Z.; Li, S.; Zhu, J.; Zou, R.; Wang, Y.; Lin, J.; Zhao, Y. *J. Power Sources* **2015**, *293*, 735–740.
- (23) Hippler, K.; Sitta, S.; Vogt, P.; Sabrowsky, H. *Acta Crystallogr., Sect. C: Cryst. Struct. Commun.* **1990**, *C46*, 736–738.
- (24) Sabrowsky, H.; Hippler, K.; Sitta, S.; Vogt, P. *Acta Crystallogr., Sect. C: Cryst. Struct. Commun.* **1990**, *C46*, 368–369.
- (25) Lu, Z.; Chen, C.; Baiyee, Z. M.; Chen, X.; Niu, C.; Ciucci, F. *Phys. Chem. Chem. Phys.* **2015**, *17*, 32547–32555.
- (26) Taniguchi, S.; Aniya, M. *IOP Conf. Ser.: Mater. Sci. Eng.* **2011**, *18*, 132016.
- (27) Lu, X.; Wu, G.; Howard, J. W.; Chen, A.; Zhao, Y.; Daemen, L. L.; Jia, Q. *Chem. Commun.* **2014**, *50*, 11520.
- (28) Mouta, R.; Melo, M. A. B.; Diniz, E. M.; Paschoal, C. W. A. *Chem. Mater.* **2014**, *26* (24), 7137–7144.
- (29) Emly, A.; Kioupakis, E.; Van der Ven, A. *Chem. Mater.* **2013**, *25* (23), 4663–4670.
- (30) Zhang, Y.; Zhao, Y.; Chen, C. *Phys. Rev. B: Condens. Matter Mater. Phys.* **2013**, *87*, 134303.
- (31) Chronos, A.; Yildiz, B.; Tarancon, A.; Parfitt, D.; Kilner, J. A. *Energy Environ. Sci.* **2011**, *4*, 2774–2789.
- (32) Neufeind, J.; Feygenson, M.; Carruth, J.; Hoffmann, R.; Chipley, K. K. *Nucl. Instrum. Methods Phys. Res., Sect. B* **2012**, *287*, 68–75.
- (33) Izumi, F.; Kawamura, Y. *Bunseki Kagaku* **2006**, *55*, 391–395.
- (34) Larson, A. C.; Von Dreele, R. B. *Los Alamos National Laboratory Report 2004*, LAUR 86-748.
- (35) Toby, B. H. *J. Appl. Crystallogr.* **2001**, *34*, 210–213.
- (36) Izumi, F.; Momma, K. *IOP Conf. Ser.: Mater. Sci. Eng.* **2011**, *18*, 022001.
- (37) Clark, S. J.; Segall, M. D.; Pickard, C. J.; Hasnip, P. J.; Probert, M. J.; Refson, K.; Payne, M. C. *Z. Kristallogr. - Cryst. Mater.* **2005**, *220*, 567.